Three-dimensional coating flow of nematic liquid crystal on an inclined substrate†

M. A. LAM[1], L. J. CUMMINGS[1], T.-S. LIN[2] and L. KONDIC[1]

[1]*Department of Mathematical Sciences and Center for Applied Mathematics and Statistics,
New Jersey Institute of Technology, Newark, NJ, 07102
email: mal37@njit.edu, Linda.Cummings@njit.edu, kondic@njit.edu*
[2]*Department of Applied Mathematics, National Chiao Tung University, 1001 Ta Heueh Road,
Hsinchu 300, Taiwan
email: tslin@math.nctu.edu.tw*

We consider a coating flow of nematic liquid crystal (NLC) fluid film on an inclined substrate. Exploiting the small aspect ratio in the geometry of interest, a fourth-order nonlinear partial differential equation is used to model the free surface evolution. Particular attention is paid to the interplay between the bulk elasticity and the anchoring conditions at the substrate and free surface. Previous results have shown that there exist two-dimensional travelling wave solutions that translate down the substrate. In contrast to the analogous Newtonian flow, such solutions may be unstable to streamwise perturbations. Extending well-known results for Newtonian flow, we analyse the stability of the front with respect to transverse perturbations. Using full numerical simulations, we validate the linear stability theory and present examples of downslope flow of nematic liquid crystal in the presence of both transverse and streamwise instabilities.

Key words: Thin films; liquid crystals; contact lines; and gravity driven flow.

1 Introduction

In many industrial applications involving fluid films, the geometry is such that the film thickness is small relative to typical lateral dimensions of the film. Exploiting this difference in scales, a long wave (lubrication) approximation to the governing equations for fluid flow may be derived and the spatial dimension of the problem reduced by one. Within this framework, the flow of thin layers (films) of fluids has been studied under a variety of physical configurations, e.g. [3, 5, 7–10, 12–18, 22, 23, 26].

Nematic liquid crystals (NLC) are fluid-like substances typically composed of rod like molecules with a dipole moment associated with the anisotropic axis (the axis parallel with the length of the rod-like molecule). The interactions of the dipole moments cause molecules to align locally, giving rise to an elastic response; however, in general, fluid flow and external forces may distort the local alignment. Therefore, liquid crystals behave as a state of matter intermediate between a fluid and a solid, having some short-range

order to their molecular structure. In addition, due to the anisotropic rheology (rod-like molecules), viscosity depends on fluid flow relative to the local orientation of molecules.

At a surface or interface, NLC molecules have a preferred orientation, a phenomenon known as anchoring. The local molecular orientation is characterized by a *director field*: a unit vector representing the average direction of the long axis of the molecules. Liquid crystal in the hybrid aligned nematic (HAN) state has a specific molecular orientation: the polar angle (with respect to the normal to the substrate), θ, of the liquid crystal molecules varies linearly over the film thickness, that is, $\theta = c_1 z + c_2$, where c_1 and c_2 are constants determined by the anchoring conditions and z is aligned with the polar axis $\theta = 0$.

This paper is a continuation of previous work [10] which focused on two-dimensional flow of NLC down an inclined substrate. Within the long wave approximation, a fourth-order nonlinear partial differential equation was derived for the evolution of the free surface height. In the absence of the contact line instability, (streamwise) instabilities are observed that appear analogous to those found for Newtonian fluid flowing down an inverted substrate [13] and flow of a Newtonian fluid on the outer surface of a vertical cylinder [17]. Using linear stability analysis, three classes of solutions were identified: Type 1, a travelling front that translates stably down the substrate; Type 2, a travelling front where instabilities occur behind the travelling front, but propagate forwards so that they are always confined to the region ahead of the initial front location (convective instability); and Type 3, instabilities propagate backwards, eventually destabilizing the entire film (absolute instability). In this paper, we examine three-dimensional flow and analyse the stability of the fluid front subject to perturbations transverse to the direction of flow. Adapting techniques applied to a Newtonian fluid [8], an asymptotic expression for the dispersion relationship is derived in the long-wavelength limit, and compared to full numerical simulations. In addition, full simulations are carried out to study the interaction of streamwise and transverse instabilities. The present work, therefore represents a three-dimensional extension of our previous work [10], which focused on the two-dimensional (streamwise) instabilities. Earlier works, such as [15], focused on spreading of NLC droplets on a horizontal substrate.

2 Governing equations

In this section, we present a long wave model for the flow of NLC down an inclined plane. The model is an asymptotic approximation to the Leslie–Ericksen equations [11], a set of partial differential equations modelling conservation of mass, momentum and energy for the NLC. The dependent variables are the velocity field, $\hat{\mathbf{v}} = (\hat{u}, \hat{v}, \hat{w})$; and the director field, $\mathbf{n} = (\sin\theta\cos\phi, \sin\theta\sin\phi, \cos\theta)$. Hatted symbols denote dimensional quantities and unaccented symbols are dimensionless. The reader is referred to our earlier work [10] for a complete derivation of the long wave model used in this paper; a brief overview is given in what follows.

The momentum equations in the Leslie–Ericksen model may be thought of as an extension to the Navier–Stokes equations, where the total stress tensor is composed of an isotropic component due to pressure, $\hat{p}$; and two anisotropic components: viscous effects, characterized by six coefficients, $\hat{\alpha}_i$ ($i = 1, 6$); and elastic response, characterized by three constants, $\hat{K}_i$ ($i = 1, 2, 3$). The elastic constants are of the same order of

magnitude, and we follow many other authors in making the so-called one constant approximation [3, 4, 15, 18, 21, 24, 27], $\hat{K} = \hat{K}_1 = \hat{K}_2 = \hat{K}_3$.

The coordinates $(\hat{x}, \hat{y}, \hat{z})$ are defined such that $(\hat{x}, \hat{y})$ are in the plane of the inclined substrate, with $\hat{x}$ pointing down the line of greatest descent, and $\hat{z}$ is normal to the substrate. The angle of inclination of the substrate to the horizontal is denoted by χ. In addition, five scaling parameters are defined: $\hat{H}$, a representative film height; $\hat{L}$, a typical lengthscale in the $\hat{x}$ direction; $\hat{U}$, a characteristic velocity in the $\hat{x}$ direction; $\hat{\mu}$, a representative viscosity scale; and $\Delta\theta$, the difference in the preferred anchoring angles at the substrate and at the free surface. Defining the fluid film aspect ratio, $\delta = \hat{H}/\hat{L} \ll 1$, we scale variables as follows:

$$(\hat{x}, \hat{y}, \hat{z}) = L(x, y, \delta z), \quad (\hat{u}, \hat{v}, \hat{w}) = U(u, v, \delta w), \quad \hat{t} = \frac{\hat{L}}{\hat{U}} t, \quad \text{and} \quad \hat{\alpha}_i = \mu \alpha_i, \tag{2.1}$$

where $\hat{\mu} = \hat{\alpha}_4/2$ is the viscosity of an analogous simple fluid i.e. with $\alpha_4 = 1$ and $\alpha_i = 0$ for $i \neq 4$, the viscous stress tensor is isotropic and models a simple fluid with viscosity $\hat{\mu}$.

We neglect inertia (which will be insignificant for the type of coating flows we consider), but retain the effects of surface tension and gravity, both of which will be important in our model. Under the scalings given by equation (2.1), five nondimensional parameters are defined: $\mathscr{B}$, the Bond number; $\mathscr{C}$, the inverse capillary number; $\mathscr{N}$, the scaled inverse Ericksen number; η, a scaled effective anisotropic viscosity; and $b \ll 1$, the dimensionless precursor layer thickness. In terms of the physical parameters, these nondimensional quantities are given by

$$\mathscr{B} = \frac{\delta^3 \hat{\rho} \hat{g} \hat{L}^2}{\hat{\mu} \hat{U}}, \quad \mathscr{C} = \frac{\delta^3 \hat{\gamma}}{\hat{\mu} \hat{U}}, \quad \mathscr{N} = \Delta\theta^2 \frac{\hat{K}}{\hat{\mu} \hat{U} \hat{L}}, \quad \eta = \frac{\hat{\alpha}_3 + \hat{\alpha}_6}{\hat{\mu}}, \quad \text{and} \quad b = \frac{\hat{b}}{\hat{H}}, \tag{2.2}$$

where $\hat{b}$ is the dimensional precursor layer thickness, $\hat{g}$ is the gravitational acceleration, $\hat{\gamma}$ is surface tension, and $\hat{\rho}$ is the density. In the present work, we consider the precursor film thickness, b, as a given parameter, fixing its value at 0.1 throughout. Detailed discussion regarding the influence of the value of b on simulation behaviour for Newtonian flows may be found in [6].

In equation (2.2), we assume elasticity is of moderate strength, $\mathscr{N} = O(\delta^0)$. One could of course consider different limits; for example strong elasticity, $\mathscr{N} = O(\delta^{-1})$; and weak elasticity, $\mathscr{N} = O(\delta)$. The case of strong elasticity is not within the scope of this paper and with the exception of neglecting lower order terms, it is unclear whether an analytically tractable model could be obtained. A weak elasticity model was considered by Carou *et al.* [1] in the framework of blade coating of a NLC.

2.1 Energetics: weak anchoring model

In the case of moderate elasticity, the time scale on which elastic reorientation occurs across the layer, $\hat{\mu} \hat{H}^2/\hat{K}$, is much faster than the time scale of fluid flow, $\hat{L}/\hat{U}$. Under this assumption, a variational approach may be used to minimize the energy with respect to variations in θ and ϕ. In the minimal energy state, the director field satisfies,

$$\phi = c_3(x, y, t), \quad \theta = c_1(x, y, t)z + c_2(x, y, t). \tag{2.3}$$

As mentioned in the Introduction, liquid crystal molecules have a preferred orientation with respect to an interface (anchoring); therefore, the functions $c_i(x, y, t)$ ($i = 1, 2, 3$) must satisfy appropriate anchoring (boundary) conditions. Two observations may be made: First, ϕ is independent of z, thus may only be determined by the anchoring imposed by the substrate or free surface. Second, in general, the anchoring condition on the polar angle θ differs between the substrate $\mathscr{S}$ and the free surface $\mathscr{F}$; therefore, for very thin films, there may be a large energy penalty in the bulk. To simplify the modelling, and in line with available experimental data, we assume that anchoring at the substrate is *planar*, and much stronger than the *homeotropic* (perpendicular) anchoring at the free surface [2, 16, 19]. Furthermore, to avoid an elastic stress singularity as the film height $h \to 0$, we allow the free surface anchoring, $\theta_{\mathscr{F}}$, to relax to the substrate anchoring, $\theta_{\mathscr{S}}$, for very thin films. Under these rather general assumptions, equation (2.3) takes the form

$$\phi = \phi_{\mathscr{S}}(x, y) \quad \text{and} \quad \theta = \theta_{\mathscr{S}} + (\theta_{\mathscr{F}} - \theta_{\mathscr{S}}) \frac{m(h)}{h} z, \tag{2.4}$$

where $m(h)$ is a monotonically increasing function such that $m(0) = 0$ and $m(\infty) = 1$. The function $m(h)$ is related to the free surface energy $\mathscr{G}(h)$[1] by [3, 10, 15],

$$\frac{\partial \mathscr{G}(h)}{\partial h} = -\mathscr{N} \frac{m(h) m'(h)}{h}. \tag{2.5}$$

We use the following functional form for $m(h)$ (see [10, 15] for motivation)

$$m(h) = f(h) \frac{h^\alpha}{h^\alpha + \beta^\alpha}, \quad f(h) = \frac{1}{2} \left[1 + \tanh \left(\frac{h - 2b}{w} \right) \right], \tag{2.6}$$

where $\alpha, \beta, w > 0$ are parameters to be chosen. The parameter β is a characteristic film thickness, above which free surface anchoring effects are dominant and below which free surface anchoring is relaxed; whereas α influences the rate of change of anchoring relaxation with respect to film height. The value of w corresponds to a characteristic range of film heights around the precursor thickness, below which free surface anchoring corresponds to that on the substrate, and above which the weak anchoring controlled by α and β applies. Note that with our chosen form of $m(h)$, the free surface energy $\mathscr{G}$ may be shown to be close to that proposed by Rapini and Papoular [20].

2.2 Long wave equation

Asymptotic reduction of the momentum equations of the Leslie–Ericksen model [11] using small aspect ratio and neglecting inertial effects, see [10] for more details, leads to the following fourth-order nonlinear partial differential equation for the free surface height, $h(x, y, t)$,

$$h_t + \nabla \cdot \left(\mathscr{C} h^3 \tilde{\nabla} \nabla^2 h - \left[\mathscr{D} h^3 + \mathscr{N} M(h) \right] \tilde{\nabla} h \right) + \mathscr{U} \mathscr{L} h^3 = 0, \tag{2.7}$$

---

[1] The more usual expression for surface energy as a function of anchoring angle at the free surface, $\mathscr{G}(\theta)$, may be obtained by use of equation (2.4).

where

$$M(h) = m^2 - hmm', \tag{2.8}$$

$$\mathscr{U} = \mathscr{B} \sin \chi, \quad \mathscr{D} = \mathscr{B} \cos \chi, \tag{2.9}$$

$$\tilde{\nabla} = \left[\lambda I + v \begin{pmatrix} \cos 2\phi & \sin 2\phi, \\ \sin 2\phi & -\cos 2\phi \end{pmatrix} \right] \begin{pmatrix} \partial_x \\ \partial_y \end{pmatrix}, \tag{2.10}$$

$$\mathscr{L} = [\lambda + v \cos 2\phi]\, \partial_x + v \sin 2\phi \partial_y + 2v[\phi_y \cos 2\phi - \phi_x \sin 2\phi], \tag{2.11}$$

$$\lambda = \frac{2 + \eta}{4(1 + \eta)}, \quad v = -\frac{\eta}{4(1 + \eta)}, \tag{2.12}$$

and $m(h)$ is defined by equation (2.6). Several properties of the above model should be noted; first, λ and v are both singular at $\eta = -1$. Furthermore, if $\eta < -1$, $\tilde{\nabla}$ has negative coefficients, which would result in surface tension having a destabilizing effect. However, for those NLCs for which data are available, $-1 < \eta < 0$; therefore, only values within this range are considered in this paper. There are two parameters in the above model that differentiate it from the analogous Newtonian model: $\mathscr{N}$, a measure of the elastic response due to the antagonistic anchoring conditions (between the free surface and substrate); and η, a measure of non-Newtonian viscous effects due to the azimuthal anchoring on the substrate, ϕ. If $\eta = \mathscr{N} = 0$, we recover a model for a Newtonian fluid; therefore, within the framework of the present model, the response due to antagonistic polar anchoring conditions and azimuthal substrate anchoring may be analysed independently.

For direct numerical simulations, the governing equation (2.7) is solved on a rectangular domain $\Omega = [x_0, x_L] \times [y_0, y_L]$. To reduce the influence of the boundaries on fluid flow, in the streamwise (x) direction the free surface height is assumed constant at the ends of the domain (modelling conditions in the far field); and in the transverse (y) direction, we prescribe periodic boundary conditions. Specifically,

$$h(x_0, y, t) = H_0, \quad h(x_L, y, t) = b, \quad h_x(x_0, y, t) = h_x(x_L, y, t) = 0, \tag{2.13}$$

$$\text{and} \quad h_y(x, y_0, t) = h_y(x, y_L, t) = h_{yyy}(x, y_0, t) = h_{yyy}(x, y_L, t) = 0, \tag{2.14}$$

where H_0 is the film thickness behind the front and b is the precursor film thickness ahead of the front. For linear stability analysis, the governing equation is solved on the unbounded domain and equation (2.13) is modified as follows:

$$h(-\infty, y, t) = H_0, \quad h(\infty, y, t) = b, \quad \text{and} \quad h_x(-\infty, y, t) = h_x(\infty, y, t) = 0. \tag{2.15}$$

The linear stability analysis assumes the solution is periodic in y.

We consider only two cases of azimuthal surface anchoring in this paper: substrate anchoring parallel to flow, $\phi = 0 \pmod \pi$; and perpendicular to flow, $\phi = \pi/2 \pmod \pi$. Note that either choice of azimuthal substrate anchoring permit two-dimensional travelling waves solutions (discussed in the following section). Under this restriction,

equations (2.10) and (2.11) simplify to

$$\tilde{\nabla} = \begin{pmatrix} \kappa_1 & 0 \\ 0 & \kappa_2 \end{pmatrix} \nabla, \quad \mathscr{L} = \kappa_1 \partial_x, \tag{2.16}$$

where

$$\kappa_1 = \begin{cases} \frac{1}{2(1+\eta)} & \phi = 0 \bmod \pi \\ \frac{1}{2} & \phi = \frac{\pi}{2} \bmod \pi \end{cases}, \quad \kappa_2 = \begin{cases} \frac{1}{2} & \phi = 0 \bmod \pi \\ \frac{1}{2(1+\eta)} & \phi = \frac{\pi}{2} \bmod \pi \end{cases}. \tag{2.17}$$

3 Two-dimensional flow revisited

For two-dimensional flow, equation (2.7) simplifies to,

$$h_t + \kappa_1 \left(\mathscr{C} h^3 h_{xxx} - \left[\mathscr{D} h^3 + \mathscr{N} M(h) \right] h_x + \mathscr{U} h^3 \right)_x = 0. \tag{3.1}$$

In previous work [10], which we now briefly review, it was shown that there exists a travelling wave solution, $h(x, t) = h_0(x - Vt) = h_0(s)$, where V is the travelling speed. The travelling solution $h_0(s)$ satisfies,

$$-V h_0 + \kappa_1 \left[\mathscr{C} h_0^3 h_0''' - \mathscr{D} h_0^3 h_0' - \mathscr{N} M(h_0) h_0' + \mathscr{U} h_0^3 \right] = c, \tag{3.2}$$

where c is a constant of integration. Imposing the far field conditions (2.15), c and V are found to satisfy

$$c = -\kappa_1 \mathscr{U} H_0 b (H_0 + b), \qquad V = \kappa_1 \mathscr{U} \left(H_0^2 + H_0 b + b^2 \right). \tag{3.3}$$

To understand the dynamics behind the travelling front, the stability of a perturbed, travelling flat film was analysed: the flat film was found to be unstable if

$$H_0^3 \mathscr{D} + \mathscr{N} M(H_0) < 0, \tag{3.4}$$

where, recall, $M(h)$ is defined by equation (2.8). Since $\mathscr{N} > 0$ the elastic response is stabilizing for $M(H_0) > 0$ and destabilizing for $M(H_0) < 0$. In the unstable regime, the growth rate of the most unstable mode is given by

$$\omega_m = \kappa_1 \frac{H_0^3}{4\mathscr{C}} \left[\mathscr{D} + \frac{\mathscr{N} M(H_0)}{H_0^3} \right]^2. \tag{3.5}$$

In addition, within the unstable regime, an expression for the velocity of the boundaries of an imposed disturbance, or wave packet, was derived,

$$\left(\frac{x}{t} \right)_\pm = 3\kappa_1 \mathscr{U} H_0^2 \pm 1.622 \kappa_1 \sqrt{-\frac{[\mathscr{D} H_0^3 + \mathscr{N} M(H_0)]^3}{\mathscr{C} H_0^3}}, \tag{3.6}$$

where '+' and '−' denote the velocity of the right and left wave packet boundaries respectively. Comparing V in equations (3.3) to (3.6), the three classes of solutions defined in [10, 14] are obtained: Type 1 (stable; $V < (x/t)_-$), Type 2 (convectively unstable;

Table 1. *Values of the parameters chosen for the simulations (except where specified otherwise). Here, Δx and Δy are the partition spacings in the x and y domains respectively*

(a) Parameters used for all simulations.

Parameter	Value	Parameter	Value	Parameter	Value
$\mathscr{C}$	2	β	0.5	Δx	0.1
$\mathscr{U}$	2	α	2	Δy	0.1
H_0	0.4	w	0.05		
b	0.1				

(b) Additional parameters for flow down an inclined substrate.

Parameter	Value
$\mathscr{D}$	1
$\mathscr{B}$	$\sqrt{5}$
χ	$\tan^{-1}(2)$

(c) Additional parameters for flow down a vertical substrate.

Parameter	Value
$\mathscr{D}$	0
$\mathscr{B}$	2
χ	$\pi/2$

Table 2. *Streamwise stability regimes in $\mathscr{N}$ domain with all other parameters fixed*

(a) Stability regimes for flow down an inclined substrate. Parameters are given in Tables 1(a) and (b).

Stability regime	Value of $\mathscr{N}$
Type 1	$\mathscr{N} < 7.1$
Type 2	$7.1 < \mathscr{N} < 11.4$
Type 3	$11.4 < \mathscr{N}$

(b) Stability regimes for flow down a vertical substrate. Parameters are given in Tables 1(a) and (c).

Stability regime	Value of $\mathscr{N}$
Type 1	$\mathscr{N} < 8.9$
Type 2	$8.9 < \mathscr{N} < 12.2$
Type 3	$12.2 < \mathscr{N}$

$0 < (x/t)_- < V$), and Type 3 (absolutely unstable; $(x/t)_- < 0$). Note that both V and $(x/t)_-$ share a common factor of κ_1, thus the transitions between stability regimes are independent of κ_1.

To simplify the parameter study when we extend our results to three-dimensional flow, we vary η, $\mathscr{N}$, and $\mathscr{D}$ and fix the remaining parameters as in Table 1(a). Furthermore, we restrict $\mathscr{D}$ (which, together with $\mathscr{U}$, fixes χ and $\mathscr{B}$, see equation (2.9)) to just two values, corresponding to flow down an inclined substrate or flow down a vertical substrate, as given in Tables 1(b) and (c), respectively. The streamwise stability regimes in the $\mathscr{N}$ domain (with other parameters as fixed in Tables 1) are given in Tables 2(a) and (b) for flow down an inclined and vertical substrate, respectively. Note that, with the chosen values of α, β, b, w, the choice of H_0 corresponds to an unstable elastic response, $M(H_0) < 0$.

4 Transverse stability of a travelling front

In this section, we expand our analysis of the two-dimensional problem [10] to three-dimensional flow; in particular, we study the transverse stability of a travelling fluid front. A travelling Newtonian front flowing down an inclined plane ($\mathscr{N} = \eta = 0, \mathscr{D} > 0$) is known to be unstable with respect to transverse perturbations [23]. With $\mathscr{U}$ fixed, increasing $\mathscr{D}$ has a stabilizing effect. Negative values of $\mathscr{D}$ (corresponding to flow on an inverted plane) have also been studied for Newtonian flow: in the two-dimensional

case [13] such flow can exhibit the Types 1, 2 and 3 streamwise instability described in Section 3, while in the three-dimensional case [14], increasing $|\mathscr{D}|$ has a destabilizing effect on transverse perturbations. We proceed to analyse transverse perturbations within the context of the present model.

Following standard techniques applied to thin films [8], we begin the analysis by assuming a solution of the form

$$h(x, y, t) = h_0(s) + \epsilon h_1(s, y, t), \qquad (4.1)$$

where $|\epsilon| \ll 1$, $s = x - Vt$, V is given by equation (3.3), $h_0(s)$ is a stable (Type 1) travelling front solution and $h_1(s, y, t)$ is a perturbation. Substituting equation (4.1) into the governing equation (2.7) and integrating with respect to s, the travelling wave equation (3.2) is obtained at the leading order. At order ϵ, we derive the following (linear) equation for h_1,

$$\frac{\partial h_1}{\partial t} + \nabla \cdot \left(\mathscr{C} \mathscr{L}_{\mathscr{C}}[h_1] - \mathscr{D} \mathscr{L}_{\mathscr{D}}[h_1] - \mathscr{N} \mathscr{L}_{\mathscr{N}}[h_1] \right) + \mathscr{U} \mathscr{L}_{\mathscr{U}}[h_1], \qquad (4.2)$$

where

$$\mathscr{L}_{\mathscr{C}} = h_0^3 \tilde{\nabla} \nabla^2 + 3 h_0^2 \tilde{\nabla} \nabla^2 h_0, \quad \mathscr{L}_{\mathscr{D}} = h_0^3 \tilde{\nabla} + 3 h_0^2 \tilde{\nabla} h_0,$$
$$\mathscr{L}_{\mathscr{N}} = M(h_0) \tilde{\nabla} + M'(h_0) \tilde{\nabla} h_0, \quad \text{and} \quad \mathscr{L}_{\mathscr{U}} = 3 h_0^2 \partial_s + 6 h_0 \partial_s h_0.$$

The operators $\mathscr{L}_i$ ($i = \mathscr{C}, \mathscr{D}, \mathscr{N}, \mathscr{U}$) are linear with respect to h_1; therefore, assuming that h_1 is a composition of Fourier modes, each mode may be considered separately, i.e. $h_1 = g(s, t) e^{iqy}$. To derive the dispersion relationship, we let $g(s, t) = \zeta(s) e^{\sigma t}$, where σ is the growth rate. Substituting this form into equation (4.2), we obtain

$$\sigma \zeta = c_4(h_0) \partial_{ssss} \zeta + c_3(h_0) \partial_{sss} \zeta + c_2(h_0; q) \partial_{ss} \zeta + c_1(h_0; q) \partial_s \zeta + c_0(h_0; q) \zeta, \qquad (4.3)$$

where

$$c_4(h_0) = -\mathscr{C} \kappa_1 h_0^3,$$
$$c_3(h_0) = -3 \mathscr{C} \kappa_1 h_0^2 \partial_s h_0,$$
$$c_2(h_0; q) = 2 \mathscr{C} \lambda q^2 h_0^3 + \kappa_1 \left[\mathscr{D} h_0^3 + \mathscr{N} M(h_0) \right],$$
$$c_1(h_0; q) = 3 \kappa_1 \left[\mathscr{C} h_0^2 \left(\partial_s h_0 q^2 - \partial_{sss} h_0 \right) + 6 \mathscr{D} h_0^2 \partial_s h_0 + 2 \mathscr{N} \partial_s h_0' M'(h_0) - 3 \mathscr{U} h_0^2 \right] + V,$$
$$c_0(h_0; q) = c_{00}(h_0; q) + c_{01}(h_0; q) + c_{03}(h_0; q) + c_{04}(h_0),$$
$$c_{00}(h_0; q) = -\mathscr{C} h_0 \left[\kappa_2 h_0^2 q^4 + \kappa_1 \left[6 \partial_s h_0 \partial_{sss} h_0 + 3 h_0 \partial_{ssss} h_0 \right] \right],$$
$$c_{01}(h_0; q) = \mathscr{D} h_0 \left[-\kappa_2 h_0^2 q^2 + \kappa_1 \left[6 \left(\partial_s h_0 \right)^2 + 3 h_0 \partial_{ss} h_0 \right] \right],$$
$$c_{02}(h_0; q) = \mathscr{N} \left[-\kappa_2 M(h_0) q^2 + \kappa_1 \left[M'(h_0) \partial_{ss} h_0 + \left(\partial_s h_0 \right)^2 M''(h_0) \right] \right],$$
$$c_{03}(h_0) = -6 \mathscr{U} \kappa_1 h_0 \partial_s h_0,$$

where λ is given by equation (2.12), and κ_i ($i = 1, 2$) by equation (2.17). To extract the growth rate, σ, for a fixed q, equation (4.3) is discretized, implementing a finite difference method to estimate the derivatives of ζ. For some partition $\{s_n\}$ of s, equation (4.3) is

approximated by

$$(A(h_0; q) - \sigma)\zeta_n = 0, \tag{4.4}$$

where $\zeta_n = \zeta(s_n)$ and $A(h_0, q)$ is the finite difference matrix. Since only the largest eigenvalue is required, a power iterative method is sufficient to calculate the growth rate for each value of q, as was done by Lin and Kondic [14].

4.1 Small wavelength approximation

To validate the results obtained by solving the eigenvalue problem (4.4), in this section we present an asymptotic approximation to the dispersion relation in the limit of small wave numbers, $|q| \ll 1$. Note that equation (4.3) contains only even powers of q; therefore, we asymptotically expand ζ and σ in q^2,

$$\sigma = \sigma_0 + q^2\sigma_1 + O(q^4) \quad \text{and} \quad \zeta = \zeta_0 + q^2\zeta_1 + O(q^4). \tag{4.5}$$

For a fixed q, the front position is modified from $s = 0$ (unperturbed) to $s = s_b(y, t) = \epsilon e^{iqy+\sigma t}$. At the front position, the film height is given by, $h(s_b, y, t) = b$. Linearizing about the unperturbed front position, $s = 0$,

$$\epsilon e^{iqy+\sigma t}\left[\zeta_0(0) - \partial_s h_0(0)\right] + O\left(\epsilon^2\right) + O\left(q^2\right) = 0. \tag{4.6}$$

Setting $\zeta_0(0) = \partial_s h_0(0)$, the boundary condition at the fluid front is satisfied to the second-order in ϵ and q. It is then reasonable to assume that $\zeta_0(s)$ takes the form

$$\zeta_0(s) = \partial_s h_0(s). \tag{4.7}$$

Substituting equations (4.5) and (4.7) into equation (4.2), order ϵq^0 terms of the dispersion relationship may be expressed as

$$\sigma_0\partial_s h_0 = \left[-Vh_0 + \kappa_1\left[\mathscr{C}h_0^3 h_0''' - \mathscr{D}h_0^3 h_0' - \mathscr{N}M(h_0)h_0' + \mathscr{U}h_0^3\right]\right]_{ss}, \tag{4.8}$$

and recalling the two-dimensional travelling wave equation, (3.2), $\sigma_0 = 0$.

To simplify the order ϵq^2 terms, it is assumed that perturbations only occur near the front position (the fluid flow is undisturbed in the far-field); therefore, subject to the boundary conditions (2.15), h_0 and ζ_1 must satisfy

$$h_0(s \to -\infty) = H_0, \quad h_0(s \to \infty) = b, \quad \text{and} \quad \zeta_1(s \to \pm\infty) = 0. \tag{4.9}$$

To proceed, we integrate the order ϵq^2 terms of equation (4.2) with respect to s over the infinite line. The majority of the terms may be integrated exactly and, applying the far field conditions (4.9), evaluate to zero. The remaining non-zero terms may be expressed as

$$\sigma_1 = \frac{\kappa_2}{H_0 - b}\int_{-\infty}^{\infty}\left[\mathscr{C}h_0^3\partial_{sss}h_0 - \mathscr{D}h_0^3\partial_s h_0 - \mathscr{N}M(h_0)\partial_s h_0\right]ds. \tag{4.10}$$

Substituting equation (3.2) in the integrand of the above expression, the small q

approximation to the dispersion relation is

$$\sigma = q^2 \frac{\kappa_2 \mathscr{U}}{H_0 - b} \int_{-\infty}^{\infty} [(h_0 - H_0)(h_0 - b)(h_0 + H_0 + b)] \, ds + O(q^4). \tag{4.11}$$

In two dimensions, κ_1 and κ_2 (which depend on η; see equation (2.17)) influence only the travelling wave speed, V, given by equation (3.3). The functional form of $H(s)$ is independent of η; hence the integral equation (4.11) does not depend on η. Note, for parallel substrate anchoring, κ_2 is a constant, thus the small q analysis is this case is independent of η. Recalling $\eta \in (-1, 0)$, we see from equation (2.17) that for perpendicular anchoring, increasing $|\eta|$ strengthens transverse instabilities.

To analyse the effect of other parameters, note that while the solution $h_0(s)$ depends on $\mathscr{C}$, $\mathscr{D}$, $\mathscr{N}$ and $\mathscr{U}$, the integrand in equation (4.11) is not directly dependent on these parameters. This suggests that the effect of these parameters on transverse stability may be predicted by knowing their influence on the shape of the travelling wave solutions, $h_0(s)$. The integrand in equation (4.11) is zero for $h_0(s) = h_0$ and $h_0(s) = b$; thus, the main contribution to the integrand comes from the region near the front. For a Newtonian fluid, increasing $\mathscr{D}$ (while keeping other parameters fixed) decreases the size of the capillary ridge in two-dimensional numerical simulations [8]. Furthermore, analysis of transverse perturbations for Newtonian fluids predicts that increasing $\mathscr{D}$ has a stabilizing effect. In the model presented, for a destabilizing elastic response in a flat film ($M(h_0) < 0$), increasing $\mathscr{N}$ increases the size of the capillary ridge in two-dimensional simulations [10]; therefore, increasing $\mathscr{N}$ is expected to have a destabilizing effect on transverse perturbations. For a stabilizing elastic response, $M(h_0) > 0$, the opposite is expected.

4.2 Influence of elastic response and substrate anchoring

To compute the growth rates predicted by the linear stability analysis, a (Type 1) travelling wave solution, $h_0(s)$, is required. Since equation (3.2) is highly nonlinear, an analytical solution is not feasible. Therefore, subject to the boundary conditions given by equation (2.13), the two-dimensional governing equation, (3.1), is evolved numerically until the initial condition has converged to a stable travelling wave. The initial condition is given by

$$h(x, 0) = \frac{(H_0 - b)}{2} \tanh[-5(x - x_f)] + \frac{H_0 + b}{2}, \quad x_f = \frac{2(x_0 + x_L)}{3}, \tag{4.12}$$

a film profile that at x_f transitions from a film of thickness h_0, to a film of thickness b, the precursor layer.

The numerical method employed to evaluate the two-dimensional governing equation, (3.1), is based on a Crank–Nicolson type discretization scheme coupled with an adaptive time stepping method. To account for the nonlinear terms, a Newton–Raphson iterative solver is implemented. The reader is referred to the paper by Lin *et al.* [15] for further information about the numerical method employed.

In addition to the small-q analysis described above, we also solve the eigenvalue problem (4.4) numerically for a range of q-values. To do this we adapt the method of Lin and Kondic [14] which computes only the largest eigenvalue σ for each value of q. As
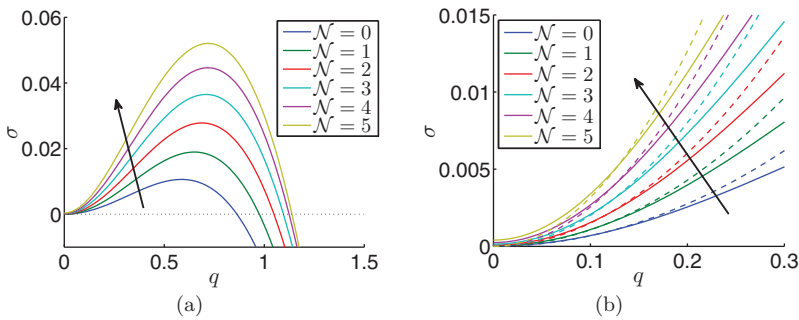
FIGURE 1. (a) Influence of $\mathcal{N}$ on the dispersion relationship as given by the numerical solution of the full eigenvalue problem, (4.4). (b) Comparison between numerical results of the eigenvalue problem (solid lines) and small-q approximation (dashed lines), (4.11). Arrows denote increasing $\mathcal{N}$. Dispersion curves ignore azimuthal substrate anchoring ($\eta = 0$) and describe flow down a vertical substrate. Parameters are given in Tables 1(a) and (c).
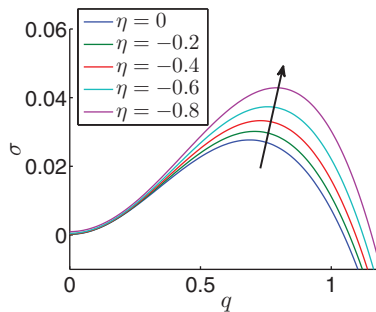

FIGURE 2. Influence of η, in the case of planar substrate anchoring parallel to the flow direction, on the dispersion relationship as given by the eigenvalue problem, (4.4). Arrow denotes the direction of increasing $|\eta|$. Here $\mathcal{N} = 2$ with other parameters given in Tables 1(a) and (c).

mentioned in Section 2.2, the effects of the elastic response, $\mathcal{N}$, and azimuthal substrate anchoring, η, may be studied independently; therefore, to begin the analysis, we consider flow down a vertical substrate with $\eta = 0$. Figure 1(a) plots the dispersion relationship for various values of $\mathcal{N}$ computed using numerical solutions to the eigenvalue problem, (4.4). The results are compared to the small-q approximations, (4.11), in Figure 1(b). It may be seen that there is a good agreement between the two methods for small q and both methods capture the expected influence of $\mathcal{N}$.

To analyse the influence of azimuthal substrate anchoring, we continue to consider flow down a vertical substrate but now fix $\mathcal{N} = 2$ and vary η. In the case of parallel anchoring, η has no influence on the small q approximation, (4.11); therefore, only the dispersion relation calculated using the eigenvalue problem, (4.4), is shown. In Figure 2, which shows the results for the case of substrate anchoring parallel to the flow direction, we observe that increasing $|\eta|$ has negligible influence for small q (as we would anticipate, since the small q analysis results were independent of η in this case); however, for larger q, increasing $|\eta|$ has a destabilizing effect. In the case of perpendicular substrate anchoring, the effect of η on the dispersion relation computed from the eigenvalue problem is shown
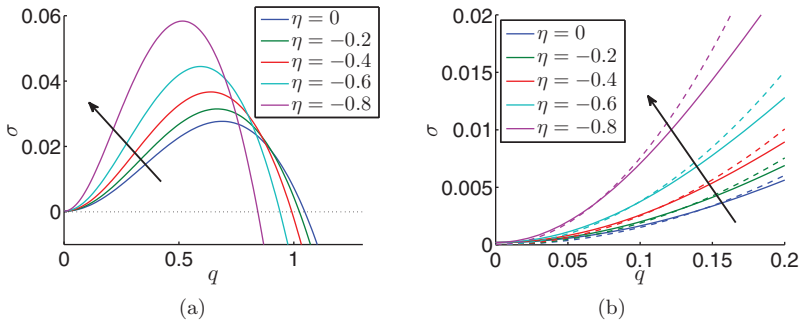
FIGURE 3. (a) Influence of η, in the case of planar substrate anchoring perpendicular to the flow direction, on the dispersion relation as given by the numerical solution of the full eigenvalue problem, (4.4). (b) Comparison between numerical results of eigenvalue problem (solid line) and small-q approximation (dashed line), (4.11). Arrows denote the direction of increasing $|\eta|$. Here $\mathcal{N} = 2$ with other parameters given in Tables 1(a) and (c).

in Figure 3(a) and compared to the small-q approximation in Figure 3(b). We observe three trends as $|\eta|$ increases: the maximum growth rate increases; the wave number, q, corresponding to the maximum growth rate decreases; and the range of unstable modes decreases.

5 Numerical simulations: three-dimensional flow

In this section, we present direct numerical simulations of equation (2.7), which describes the evolution of the free surface for NLC flowing down an incline. We implement an Alternating Direction Implicit (ADI) type method with adaptive time stepping; see [14] for the details of implementation, and [25] for a more general discussion of the use of ADI method in the context of nonlinear high-order parabolic equations. To reduce the size of the computational domain, the grid is expanded dynamically in the streamwise (x) direction such that the free surface height is always sufficiently flat at the boundaries of the computational domain. The grid is shifted so that the lengths of the flat regions at the boundaries are equal. This corresponds to undisturbed flow at the boundaries (2.13). The initial length of the x domain, $L_x = x_L - x_0$, is fixed at $L_x = 40$ for all simulations. In the y direction, symmetry boundary conditions are imposed. The length of the y domain is fixed according to the initial condition of interest.

To generate an initial condition, for a fixed y, the numerical travelling wave solution is shifted and then interpolated to an equispaced (x, y) grid. Specifically, if $\{\hat{x}_i\}$ is the partition of the travelling wave solution, the shifted partition is defined as $\tilde{x}_i(y) = \hat{x}_i + \Delta x_f(y)$, where $\Delta x_f(y)$ is the perturbation to the front position. Using cubic splines, the solution at nodes $\{\tilde{x}_i(y)\}$ is interpolated to an equispaced partition, $\{x_j\}$. This is equivalent to

$$h(x, y, t = 0) = h_0(x - \Delta x_f(y)). \tag{5.1}$$

In addition, the initial condition is shifted such that the initial unperturbed front position, x_{f0}, is the same for all simulations i.e. $x_f(y) = x_{f0} + \Delta x_f(y)$, where $x_{f0} = 24$.

To analyse transverse instabilities, we fix the length of the y domain to be one wavelength of a plane wave, i.e.

$$x_f(y) = -A \cos(q[y - y_0]), \quad q = \frac{2\pi}{y_L - y_0}, \tag{5.2}$$

where $A = 0.1$ is the magnitude of the perturbation and for simplicity $y_0 = 0$. Furthermore, with the exception of extracting growth rates to validate the dispersion relation for different q, y_L is set to correspond approximately to the most unstable mode for the Newtonian case ($\mathcal{N} = 0$ and $\eta = 0$). Specifically, for flow down an inclined substrate, $y_L = 13$, and for flow on a vertical substrate, $y_L = 11$.

To simulate coating flows that appear in practice, we also consider the flow of a NLC on a wider y domain. In this case, the front position is perturbed by a superposition of cosine waves with random coefficients. Specifically, the perturbed front position and y domain are defined as

$$x_f(y) = \sum_{n=1}^{N=20} a_n \cos(q_n[y - y_0]), \quad q_n = \frac{n\pi}{y_L - y_0}, \quad y_L = 100, \tag{5.3}$$

where a_n are randomly chosen in the interval $[-0.1, 0.1]$.

Note that with double precision arithmetic (round-off error on the scale of 10^{-16}), numerical noise is expected to grow on the time scale

$$T_M = \frac{14 \ln 10}{\tau}, \tag{5.4}$$

where τ is the growth rate of an instability (streamwise or transverse). It is assumed that numerical noise becomes significant when the magnitude of numerical noise instability grows to that of the numerical accuracy of the ADI method, $\Delta x^2 = \Delta y^2 = 0.01$. Our simulations focus on the time scales that are short compared to T_M and therefore numerical noise is not expected to influence the results.

5.1 Streamwise stable flow (Type 1)

In this section, we present numerical simulations of a Newtonian flow and a NLC flow in the Type 1 regime (stable to streamwise perturbations), on an inclined and vertical substrate. The influence of the azimuthal anchoring is ignored, $\eta = 0$. The height profiles of a Newtonian flow on a vertical substrate ($\mathcal{D} = 0$) are shown in Figure 4. It is observed that the initial perturbation present in Figure 4(a) grows into a finger, which eventually evolves to a stable size and then translates steadily down the substrate. The existence of the steady travelling solution may be similar as discussed in [9], where it is predicted that stable nontrivial travelling waves may exist for certain parameter values. Analysis of this phenomenon is not within the scope of this paper and we refer the reader to [9] for further discussion. Figure 5 shows the corresponding results for a film of NLC, with $\mathcal{N} = 2$. Initially a single central finger forms and at later times, secondary fingers evolve along the y boundaries. Recalling Figure 1(a), for $\mathcal{N} = 2$, the critical wavelength is
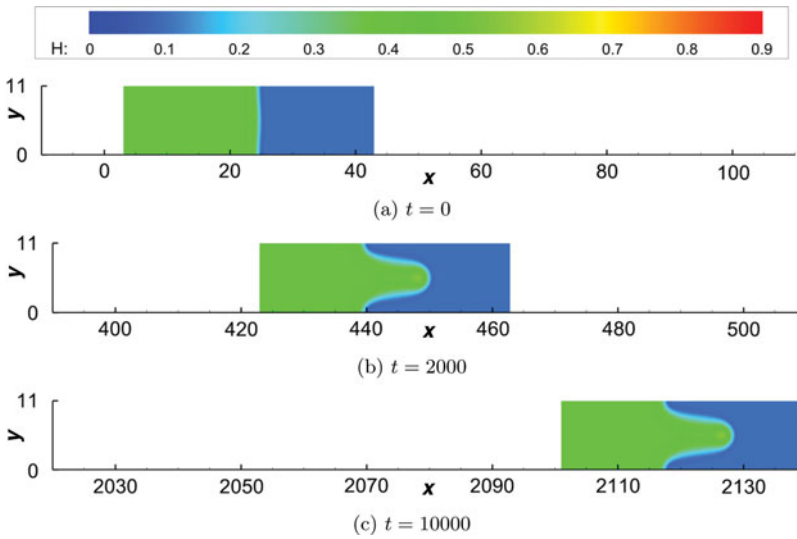
FIGURE 4. Height profile of a Newtonian ($\mathcal{N} = 0$ and $\eta = 0$) flow down a vertical substrate ($\mathcal{D} = 0$) at various times. $T_M = 3{,}000$ and other parameters are given in Tables 1(a) and (c).
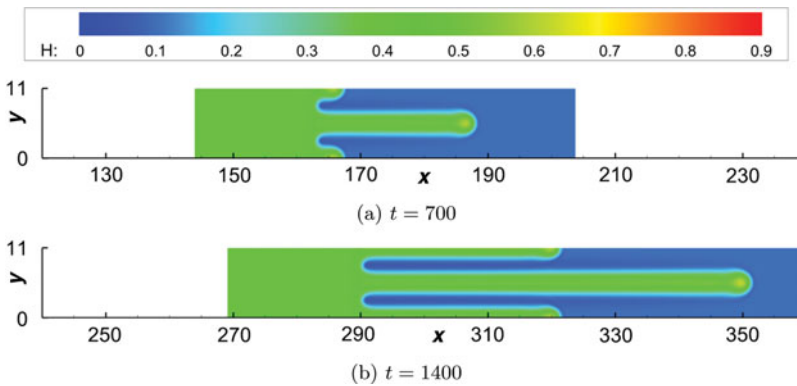

FIGURE 5. Height profile of a Type 1 ($\mathcal{N} = 2$) flow down a vertical substrate ($\mathcal{D} = 0$) at various times. Here the azimuthal substrate anchoring is ignored ($\eta = 0$), and other parameters are given in Tables 1(a) and (c). The initial front position, $x_f \approx 24$, and the initial condition is similar to Figure 4(a).

approximately 6. This suggests that the y domain, $0 \leqslant y \leqslant 11$, is large enough to allow other modes (secondary fingers) to develop.

Figure 6 shows the results for Newtonian and Type 1 NLC flow down an inclined substrate ($\mathcal{D} = 1$). The dynamics are qualitatively similar to those for the vertical substrate, hence we show film height profiles only at the final time, corresponding to the solution snapshots of Figures 4(c) and 5(b). Increasing $\mathcal{D}$ is observed to have stabilizing effect, as evidenced by the smaller finger lengths observed in Figure 6.
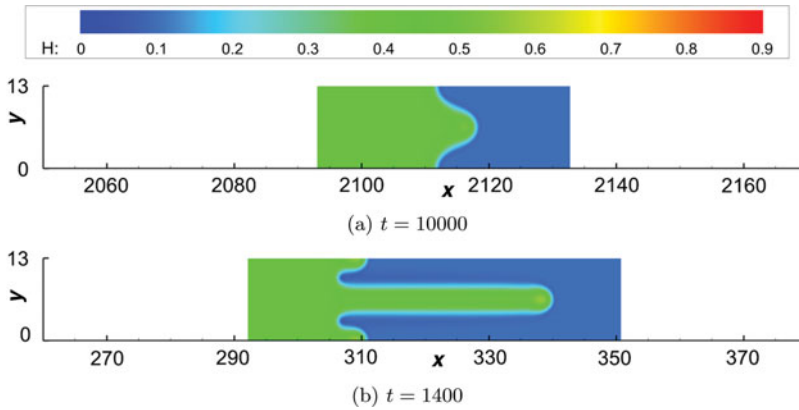
FIGURE 6. Height profiles of (a) Newtonian ($\mathcal{N} = 0$ and $\eta = 0$) flow; and (b) Type 1 ($\mathcal{N} = 2$) flow down an inclined substrate ($\mathcal{D} = 1$) where the azimuthal substrate anchoring is ignored ($\eta = 0$). For earlier times, the evolution of the height profile are qualitatively similar to Figures 4 and 5. Other parameters are given in Tables 1(a) and (b).

5.1.1 *Growth rate of transverse perturbations*

To extract the growth rate from simulation results, we track the position (along the x-axis) of the central finger's tip and root, $x_t(t)$ and $x_r(t)$, respectively. The location of the centre of the finger is defined as $x_c(t) = [x_t(t) + x_r(t)]/2$, and the length of the finger as $L(t) = x_t(t) - x_r(t)$. Following the investigation of Section 4.2, we first consider flow down a vertical substrate where the azimuthal substrate anchoring is ignored ($\eta = 0$) and vary the elastic response parameter, $\mathcal{N}$.

Changing the reference frame to one moving with the speed of the two-dimensional travelling wave, V given in equation (3.3), the position of the fingertip and root are shown in Figures 7(a) and (b). It may be seen that there exist at least two spreading regimes; initially, the fingertip and root travel at velocities close to the two-dimensional travelling wave speed, V. As the finger evolves, the velocities deviate from V, but appear to be nearly constant in time. The centre of the finger, $x_c(t)$, in the reference frame of the travelling wave, is shown in Figure 7(c). At first, the centre of the finger travels at the two-dimensional travelling wave speed, suggesting that the velocities of the fingertip and root are equal but opposite. For later times, the finger centre velocity may vary depending on the value of $\mathcal{N}$; however, the centre of the finger always remains near the two-dimensional travelling wave front position. This suggests that while the tip of the finger travels further down the substrate than the two-dimensional travelling wave solution, the area of the substrate coated by a film of uniform thickness is less than it would be if the film were stable with respect to transverse perturbations.

Figure 7(d) plots the finger length normalized by the initial length, $L_0 = 2A = 0.2$, on a semi-log scale. It may be seen that initially fingers grow exponentially in time, as anticipated, but at later times, growth rates decrease. Extracting the growth rate, σ, from the linear regions observed in Figure 7(d), the dispersion relation found numerically by solving equation (4.4) may be validated. To proceed, we consider a Type 1 flow ($\mathcal{N} = 2$) with three types of azimuthal substrate anchoring: substrate anchoring where
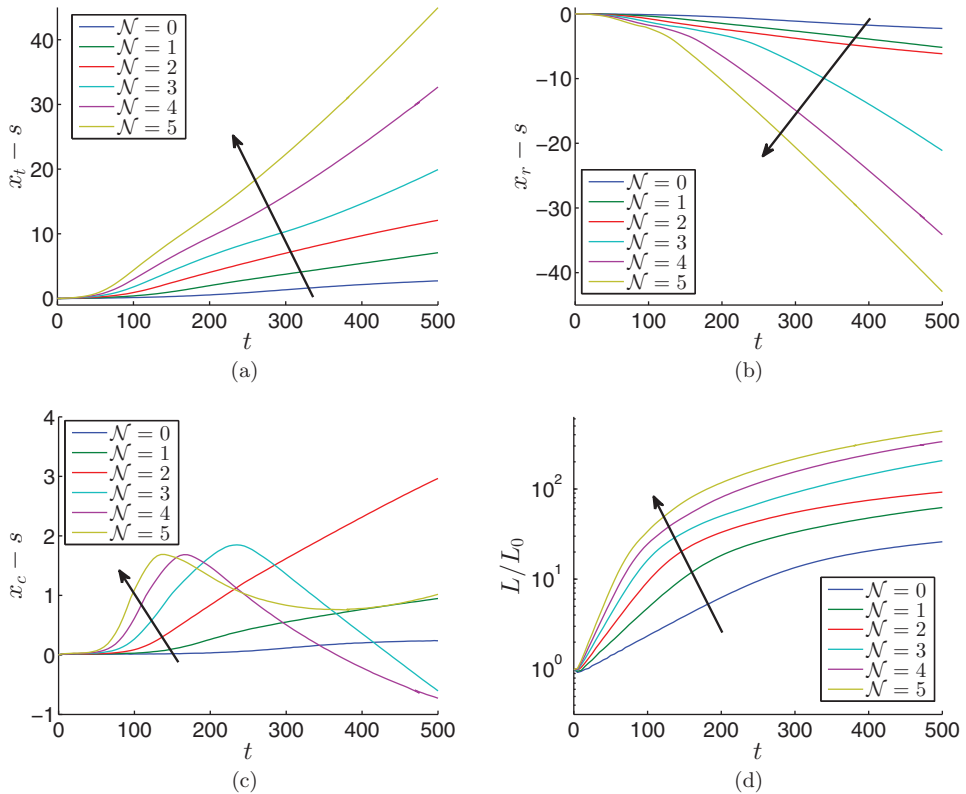
FIGURE 7. Effect of $\mathcal{N}$ on (a) position of perturbation tip, (b) position of perturbation root, (c) centre of perturbation and (d) length of perturbation. The arrows denote increase of $\mathcal{N}$. Note the positions in (a), (b) and (c) are plotted in the reference frame $x - s = x - Vt$ where $V = 0.21$, given by equation (3.3). Here $\eta = 0$ and other parameters are given by Tables 1(a) and (c).

the azimuthal angle is ignored ($\eta = 0$), planar substrate anchoring that is parallel to flow with $\eta = -0.8$, and planar substrate anchoring that is perpendicular to flow with $\eta = -0.8$. Figure 8 shows that there is excellent agreement between growth rates extracted from direct simulations of equation (4.4), and the growth-rate given by numerically solving the discretized eigenvalue problem for all three cases considered. These results validate the influence of η and $\mathcal{N}$ on transverse stability predicted by the eigenvalue problem in the both cases of the azimuthal substrate anchoring.

5.2 Streamwise and transverse instability (Type 2 and Type 3)

In this subsection, we discuss several numerical simulations where transverse and streamwise instabilities are present simultaneously. We ignore the azimuthal substrate anchoring initially and consider flow down a vertical substrate ($\mathcal{D} = 0$) and inclined substrate ($\mathcal{D} = 1$). The values of $\mathcal{N}$ are chosen such that either Type 2 or Type 3 solutions are expected [10] (see Table 2). Other parameters are given in Table 1. In the case of a vertical substrate (Table 1(c)), Figures 9 and 10 show the evolution of the free surface height for a Type 2 flow ($\mathcal{N} = 9$) and Type 3 flow ($\mathcal{N} = 12$), respectively. For flow down an inclined
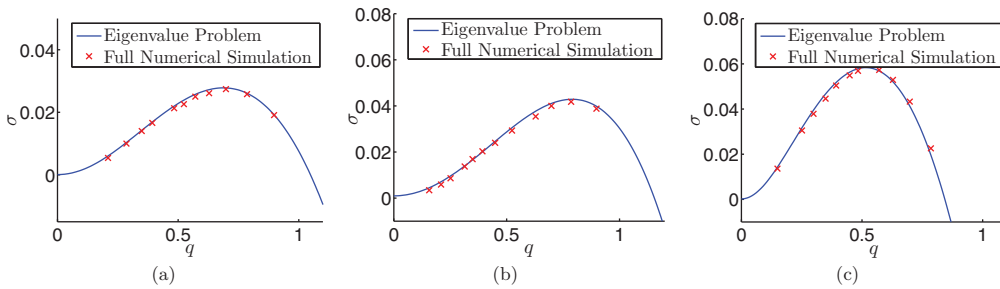
FIGURE 8. Comparison of dispersion relation computed using the eigenvalue problem (4.4) and growth rate extracted from direct numerical simulations, described in Section 5.1.1. Dispersion curves are calculated for a Type 1 ($\mathcal{N} = 2$) down a vertical substrate where (a) azimuthal substrate anchoring has been ignored ($\eta = 0$), (b) parallel azimuthal substrate anchoring with $\eta = -0.8$ and (c) perpendicular azimuthal substrate anchoring with $\eta = -0.8$. Other parameters are given in Tables 1(b) and (c).

substrate (Table 1(b)), the evolution of the height profiles for Type 2 flow ($\mathcal{N} = 10$) and Type 3 flow ($\mathcal{N} = 16$) is shown in Figures 11 and 12, respectively. Comparing the numerical results, first note the initial perturbed front position, $x_f \approx 24$, relative to the unstable region. For Type 2 flows, it is expected that the streamwise instability behind the front does not propagate (in the x direction) beyond the initial front position; Figures 9 and 11 confirm this expectation. By contrast, Figures 10 and 12 show that for a Type 3 flow, the streamwise instabilities propagate beyond the initial front position, a result expected from the two-dimensional analysis (presented in detail in [10] and summarized in Section 3). These results suggest that the classifications of solutions in two dimensions (Type 1, 2 and 3) carry over to the three-dimensional case.

In the simulations presented, we observe two types of qualitative dynamics: tear formation (e.g. $x \approx 80$ in Figure 9(a)) and semi-stable travelling ridges (e.g. $x \approx 40$ in Figure 12(a)). Examining Figures 9–11, it may be seen that streamwise instabilities occur behind the front, resulting in dewetting in the centre. The dewetted region grows in the x and y directions, resulting in the initial finger breaking from the front, forming a tear like shape. Behind the dewetting region, analogous instabilities occur near the y boundaries and form secondary tears. This process alternates between the two types of tear formation. Newly formed tears appear to briefly accelerate after breakup; however, tears will eventually elongate and connect with other tears in the streamwise direction. Considering a larger domain in the y-direction, Figure 13 shows the height profiles for a Type 3 flow down a vertical substrate where the front position has been perturbed by the superposition of cosine waves with random coefficients (see equation (5.3)). It may be seen that similar tear formation occurs.

For a Type 3 flow down an inclined substrate, Figure 12, we observe the formation of travelling ridges behind the front. The ridges appear to be analogous to solitary-like waves observed in two-dimensional simulations [10, 13]. Similarly to the tear formation flows, streamwise instabilities occur behind the front; however, the dewetting regions grow rapidly in the transverse direction, splitting the film in the streamwise direction. This may be seen in Figure 12(a), where the dewetted region behind the newly forming ridge is
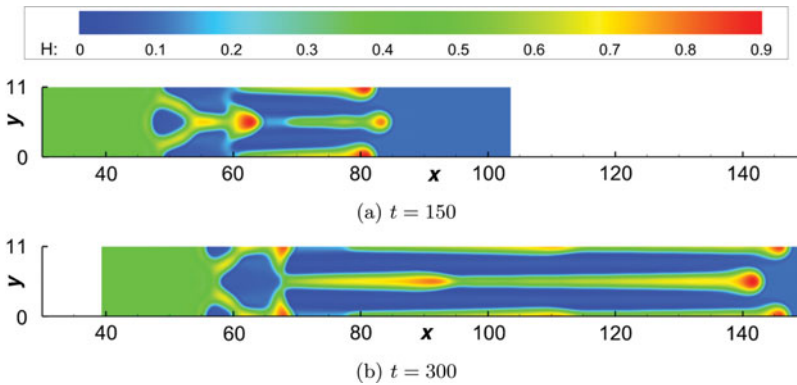
FIGURE 9. Height profile of a Type 2 ($\mathcal{N} = 9$) flow down a vertical substrate at various times. Here the azimuthal substrate anchoring is ignored ($\eta = 0$), and other parameters are given in Tables 1(a) and (c). The initial front position, $x_f \approx 24$, and the initial condition is similar to Figure 4(a).
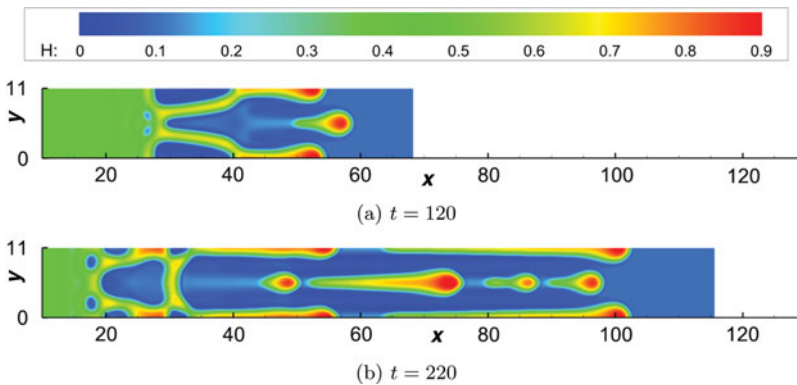

FIGURE 10. Height profile of a Type 3 ($\mathcal{N} = 12$) flow down a vertical substrate at various times. Here the azimuthal substrate anchoring is ignored ($\eta = 0$), and other parameters are given in Tables 1(a) and (c). The initial front position, $x_f \approx 24$, and the initial condition is similar to Figure 4(a).

elongated. This suggests that the instability in the streamwise direction is stronger than the instability in the transverse direction. Newly formed ridges, however, do not persist and eventually destabilize in the transverse direction. For later times, Figure 12(b), it appears that the formation of new ridges terminates. Simulating this type of flow on a larger y domain with a randomly-perturbed front position, Figure 14 shows that ridge formation still occurs for a Type 3 flow down an inclined surface.

The existence of the semi-stable travelling ridges may be due to the initial competition between transverse instability and streamwise instability. When tear formation is observed, Figure 12, the transverse perturbation of the front grows by a non-negligible amount before the streamwise instability occurs. In the case of ridge formation, the streamwise instability occurs well before the transverse perturbation has time to grow sufficiently. This suggests that instability is stronger in the streamwise direction, which is supported by the rapid breakup observed in the x direction. Therefore, initially, the shape of the patterns that
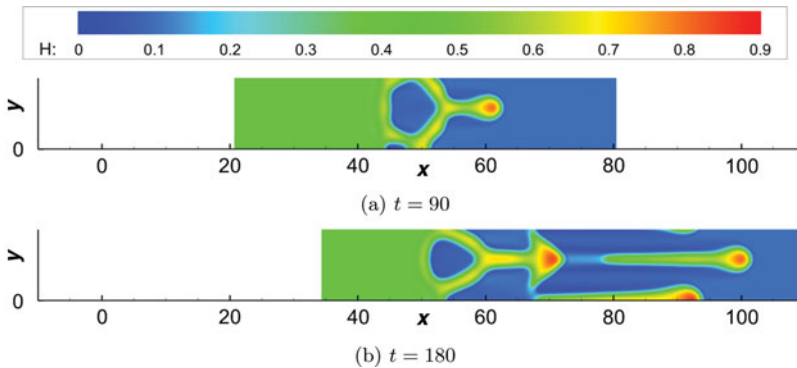
FIGURE 11. Height profile of a Type 2 ($\mathcal{N} = 10$) flow down an inclined substrate at various times. Here the azimuthal substrate anchoring is ignored ($\eta = 0$), and other parameters are given in Tables 1(a) and (b). The initial front position, $x_f \approx 24$, and the initial condition is similar to Figure 4(a).
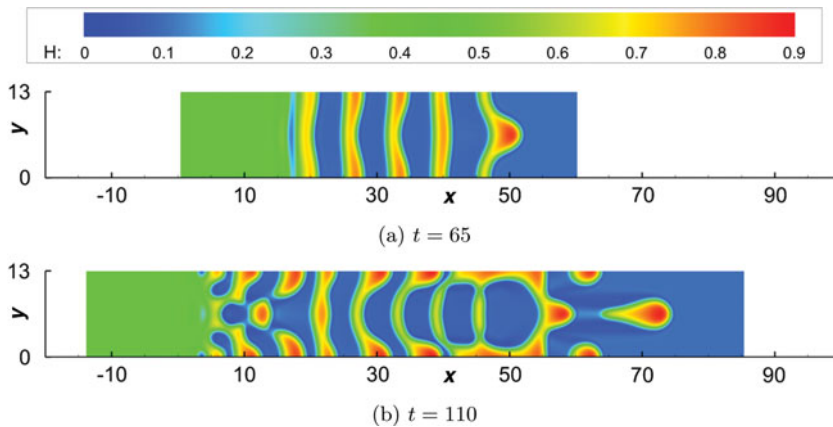

FIGURE 12. Height profile of a Type 3 ($\mathcal{N} = 16$) flow down an inclined substrate at various times. Here the azimuthal substrate anchoring is ignored ($\eta = 0$), and other parameters are given in Tables 1(a) and (b). The initial front position, $x_f \approx 24$, and the initial condition is similar to Figure 4(a).

form behind the front seems to be governed by the streamwise instability. This results in a film profile that is similar to two-dimensional solutions, but has been extended and perturbed in the y direction. For later times, the ridges destabilize at a rate similar to that of the originally perturbed front.

5.2.1 *Influence of azimuthal substrate anchoring*

For a spreading NLC drop on a horizontal substrate, it is known that, for radially-asymmetric azimuthal substrate anchoring $\phi(x, y)$, the anchoring pattern imposed on the substrate is reflected in the shape and structure of the spreading droplet [15]: broadly speaking, for planar substrate anchoring patterns the flow is fastest in the direction parallel to the anchoring direction, and slowest in the direction perpendicular to the anchoring.
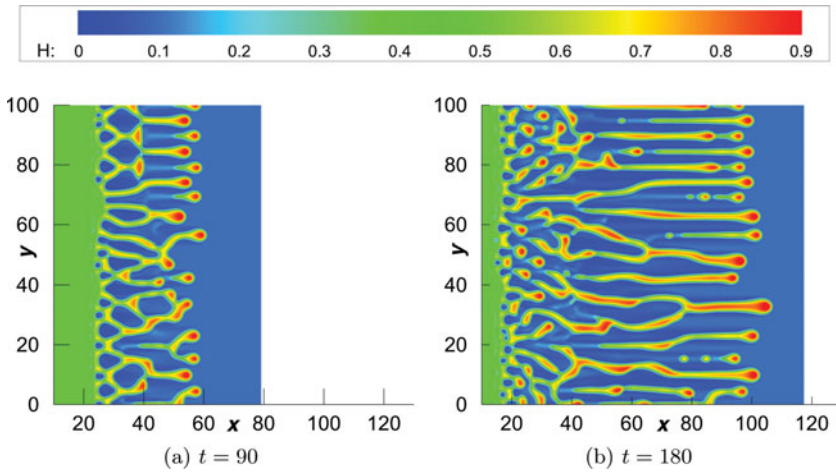
FIGURE 13. Height profile of a Type 3 ($\mathcal{N} = 12$) flow down a vertical substrate ($\mathcal{D} = 0$) at various times. Here the azimuthal substrate anchoring is ignored ($\eta = 0$) and other parameters are given in Tables 1(a) and (c). The initial front position, $x_{f0} = 24$.
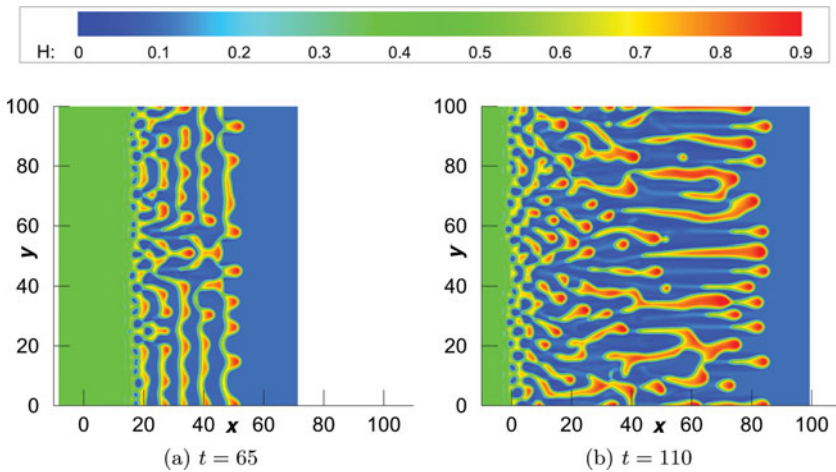

FIGURE 14. Height profile of a Type 3 ($\mathcal{N} = 16$) flow down a inclined substrate ($\mathcal{D} = 1$) at various times. Here the azimuthal substrate anchoring is ignored ($\eta = 0$) and other parameters are given in Tables 1(a) and (b). The initial front position, $x_{f0} = 24$.

Figures 15 and 16 show the influence of parallel and perpendicular substrate anchoring, respectively, on a Type 2 flow down a vertical substrate ($\mathcal{N} = 9$) for various values of η. For the parameters considered, the height profiles at $t = 80$ are shown in Figures 15 and 16. In the case of parallel substrate anchoring, Figure 15 shows that increasing $|\eta|$ elongates the finger in the direction of anchoring. For perpendicular substrate anchoring, it may be seen that structure behind the finger, observed in Figure 16(a), is destroyed in Figures 16(b) and (c). Given that tear formation eventually occurs, the earlier onset of the breakup suggests that increasing $|\eta|$ strengthens the instability in the transverse direction.
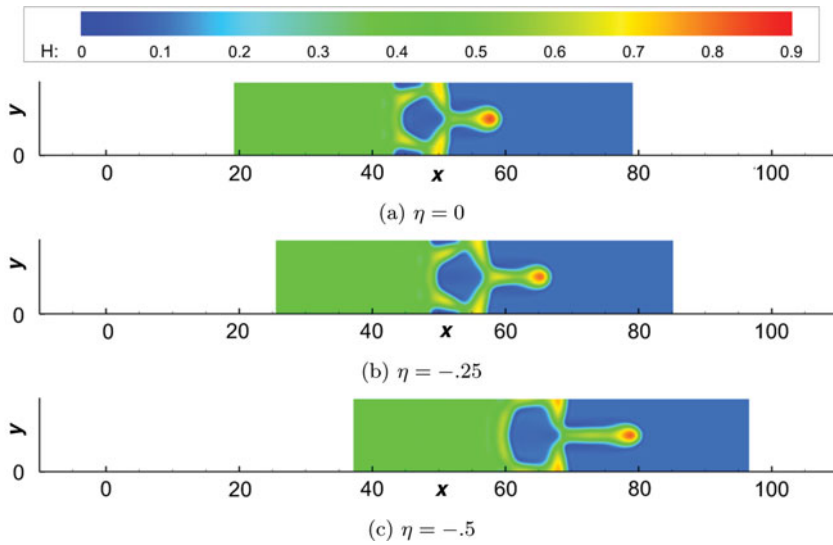
FIGURE 15. Influence of η and parallel azimuthal substrate anchoring on the evolution of the height profile of a Type 2 flow ($\mathcal{N} = 9$) down a vertical substrate. Height profiles are at a fixed later time, $t = 80$. Other parameters are given in Tables 1(a) and (c).

FIGURE 16. Influence of η and perpendicular azimuthal substrate anchoring on the evolution of the height profile of a Type 2 flow ($\mathcal{N} = 9$) down a vertical substrate. Height profiles are at a fixed later time, $t = 80$. Other parameters are given in Tables 1(a) and (c).
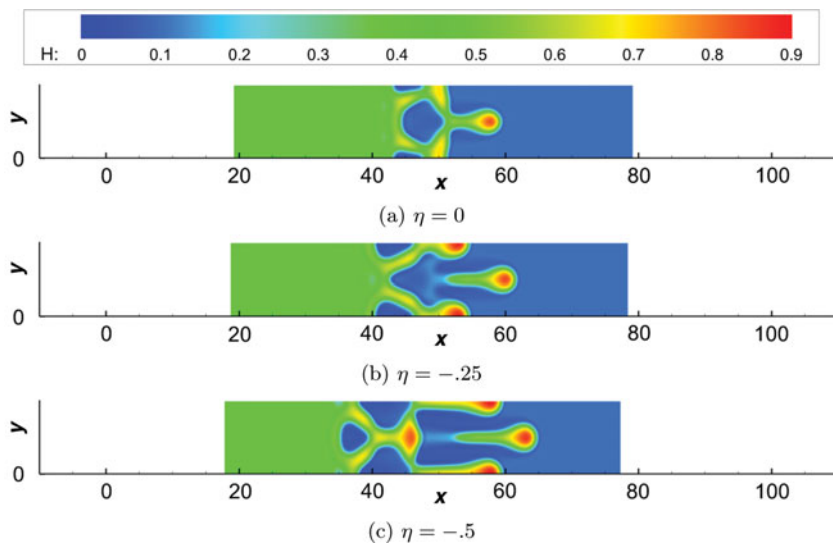
6 Conclusions

To summarize, we have analysed the flow of a NLC film down an inclined substrate, with weak homeotropic anchoring at the free surface, and strong planar anchoring at the substrate. Two specific cases of substrate anchoring were considered: parallel or

perpendicular to the streamwise direction. The model we derive admits two-dimensional travelling waves for these simple anchoring scenarios. These travelling waves may be unstable to both transverse and streamwise perturbations. For flows that are streamwise stable, we have derived an asymptotic approximation to the dispersion relationship for transverse perturbations and validated the analysis by extracting the growth rates of transverse perturbations from direct numerical simulation of the governing equation. In the presence of streamwise and transverse instabilities, we observe rich dynamics when considering the evolution of the free surface height. In addition, simulations suggest that the influence of azimuthal substrate anchoring is similar to that observed for spreading NLC drops on a horizontal substrate [15]. We hope that our computational results will inspire future experimental investigations that may provide additional insight regarding the model used.

References

[1] Carou, J., Mottram, N., Wilson, S. & Duffy, B. (2007) A mathematical model for blade coating of a nematic liquid crystal. *Liq. Cryst.* **35**, 621.

[2] Cazabat, A. M., Delabre, U., Richard, C. & Sang, Y. Y. C. (2011) Experimental study of hybrid nematic wetting films. *Adv. Colloid Interface Sci.* **168**, 29.

[3] Cummings, L. J., Lin, T.-S. & Kondic, L. (2011) Modeling and simulations of the spreading and destabilization of nematic droplets. *Phys. Fluids* **23**, 043102.

[4] Delabre, U., Richard, C. & Cazabat, A. M. (2009) Thin nematic films on liquid substrates. *J. Phys. Chem. B* **113**, 3647.

[5] Diez, J. A., González, A. G. & Kondic, L. (2009) On the breakup of fluid rivulets. *Phys. Fluids* **21**, 082105.

[6] Diez, J. A., Kondic, L. & Bertozzi, A. (2000) Global models for moving contact lines. *Phys. Rev. E* **63**, 011208.

[7] Ehrhand, P. & Davis, S. H. (1991) Non-isothermal spreading of liquid drops on horizontal plates. *J. Fluid Mech.* **229**, 365.

[8] Kondic, L. (2003) Instabilities in gravity driven flow of thin fluid films. *SIAM Rev.* **45**, 95.

[9] Kondic, L. & Diez, J. (2005) On nontrivial traveling waves in thin film flows including contact lines. *Physica D* **209**, 135-144.

[10] Lam, M. A., Cummings, L. J., Lin, T.-S. & Kondic, L. (2014) Modeling flow of nematic liquid crystal down an incline. *J. Eng. Math.* doi: 10.1007/s10665-014-9697-2.

[11] Leslie, F. M. (1979) Theory of flow phenomena in liquid crystals. *Adv. Liq. Cryst.* **4**, 1.

[12] Lin, T.-S., Cummings, L. J., Archer, A. J., Kondic, L. & Thiele, U. (2013) Note on the hydrodynamic description of thin nematic films: Strong anchoring model. *Phys. Fluids* **25**, 082102.

[13] Lin, T.-S. & Kondic, L. (2010) Thin films flowing down inverted substrates: Two dimensional flow. *Phys. Fluids* **22**, 052105.

[14] Lin, T.-S., Kondic, L. & Filippov, A. (2012) Thin films flowing down inverted substrates: Three-dimensional flow. *Phys. Fluids* **24**, 022105.

[15] Lin, T.-S., Kondic, L., Thiele, U. & Cummings, L. J. (2013) Modeling spreading dynamics of liquid crystals in three spatial dimensions. *J. Fluid Mech.* **729**, 214.

[16] Manyuhina, O. V. & Ben Amar, M. (2013) Thin nematic films: Anchoring effects and stripe instability revisited. *Phys. Lett. A* **377**, 1003.

[17] Mayo, L. C., McCue, S. W. & Moroney, T. J. (2013) Gravity-driven fingering simulations for a thin liquid film flowing down the outside of a vertical cylinder. *Phys. Rev. E* **87**, 053018.

[18] NAUGHTON, S. P., PATEL, N. K., SERIC, I., KONDIC, L., LIN, T.-S. & CUMMINGS, L. J. (2013) Instability of gravity driven flow of liquid crystal films. *SIAM Undergrad. Res. Online* **5**, 56.

[19] POULARD, C. & CAZABAT, A. M. (2003) Spontaneous spreading of nematic liquid crystals. *Langmuir* **21**, 6270.

[20] RAPINI, A. & PAPOULAR, M. (1969) Distorsion d'une lamelle nèmatique sous champ magnètique conditions d'ancrage aux parios. *J. Phys. Colloques* **30**, C4-54.

[21] REY, A. D. (2008) Generalized young-laplace equation for nematic liquid crystal interfaces and its application to free-surface defects. *Mol. Cryst. Liq. Cryst.* **369**, 63.

[22] THIELE, U., ARCHER, A. J. & PLAPP, M. (2012) Thermodynamically consistent description of the hydrodynamics of free surfaces covered by insoluble surfactants of high concentration. *Phys. Fluids* **24**, 102107.

[23] TROIAN, S. M., HERBOLZHEIMER, E., SAFRAN, S. A. & JOANNY, J. F. (1989) Fingering instabilities of driven spreading films. *Europhys. Lett.* **10**, 25.

[24] VAN EFFENTERRE, D. & VALIGNAT, M. P. (2003) Stability of thin nematic films. *Eur. Phys. J. E* **12**, 367.

[25] WITELSKI, T. & BOWEN, M. (2003) ADI schemes for higher-order nonlinear diffusion equations. *Appl. Num. Math.* **45**, 331.

[26] YANG, L. & HOMSY, G. M. (2007) Capillary instabilities of liquid films inside a wedge. *Phys. Fluids* **19**, 044101.

[27] ZIHERL, P. & ZUMER, S. (2003) Morphology and structure of thin liquid-crystalline films at nematic-isotropic transition. *Eur. Phys. J. E* **12**, 361.